Electronic conductivity of solid and liquid (Mg, Fe)O computed from first principles

E. Holmström [a,b], L. Stixrude [a,*], R. Scipioni [a], A.S. Foster [b,c]

[a] Department of Earth Sciences, University College London, Gower Street, London WC1E 6BT, UK
[b] Department of Applied Physics, COMP Centre of Excellence, Aalto University, P.O. Box 11100, 00076 Aalto, Espoo, Finland
[c] Division of Electrical Engineering and Computer Science, Kanazawa University, Kanazawa 920-1192, Japan

A B S T R A C T

Ferropericlase $(Mg, Fe)O$ is an abundant mineral of Earth's lower mantle and the liquid phase of the material was an important component of the early magma ocean. Using quantum-mechanical, finite-temperature density-functional theory calculations, we compute the electronic component of the electrical and thermal conductivity of $(Mg_{0.75}, Fe_{0.25})O$ crystal and liquid over a wide range of planetary conditions: 0–200 GPa, 2000–4000 K for the crystal, and 0–300 GPa, 4000–10,000 K for the liquid. We find that the crystal and liquid are semi-metallic over the entire range studied: the crystal has an electrical conductivity exceeding 10^3 S/m, whereas that of the liquid exceeds 10^4 S/m. Our results on the crystal are in reasonable agreement with experimental measurements of the electrical conductivity of ferropericlase once we account for the dependence of conductivity on iron content. We find that a harzburgite-dominated mantle with ferropericlase in combination with Al-free bridgmanite agrees well with electromagnetic sounding observations, while a pyrolitic mantle with a ferric-iron rich bridgmanite composition yields a lower mantle that is too conductive. The electronic component of thermal conductivity of ferropericlase with $X_{Fe} = 0.19$ is negligible (<1 W/m/K). The electrical conductivity of the crystal and liquid at conditions of the core-mantle boundary are similar to each other (3×10^4 S/m). A crystalline or liquid ferropericlase-rich layer of a few km thickness thus accounts for the high conductance that has been proposed to explain anomalies in Earth's nutation. The electrical conductivity of liquid ferropericlase exceeds that of liquid silica by more than an order of magnitude at conditions of a putative basal magma ocean, thus strengthening arguments that the basal magma ocean could have produced an ancient dynamo.

© 2018 Published by Elsevier B.V.

1. Introduction

Constraining the transport properties of planetary materials is of paramount importance for understanding the history, dynamics, and evolution of planets. The electrical and thermal conductivity of Earth are intimately linked to the age of Earth's solid inner core and the geodynamo, as well as coupling of the core and mantle (Buffett, 1992) and patterns of mantle convection (Stackhouse et al., 2015). Furthermore, the transport properties of candidate planetary materials can be used to place constraints on the composition of our planet when compared to geophysical observations of mantle conductivity (Püthe et al., 2015).

Laboratory measurements of the electrical conductivity of the major lower-mantle components $(Mg, Fe)O$ and $(Mg, Fe)SiO_3$ have provided valuable information (Li and Jeanloz, 1990; Dobson and Brodholt, 2000; Ohta et al., 2010, 2017), but conditions at the core-mantle boundary (CMB) remain unattained in experiment. The lattice component of thermal conductivity for these materials has been constrained reasonably well (Stackhouse et al., 2010; Ohta et al., 2017), but the possible significance of the electronic component has received little attention to date (Ohta et al., 2017). In addition, the conductivity of terrestial planetary materials in their molten state is of great interest, regarding in particular the question of a dynamo mechanism based in a magma ocean on Earth-like planets (Ziegler and Stegman, 2013). No experimental measurements of electrical conductivity of oxide or silicate liquids are available at deep magma ocean conditions. We have previously predicted the electrical conductivity of SiO_2 at high pressure and temperature (Scipioni et al., 2017), but the effect of other major magma ocean components, such as MgO or FeO, is unknown.

To address these shortcomings, we compute the electronic component of the electrical and thermal conductivity of $(Mg_{0.75}, Fe_{0.25})O$ from first principles in both the crystalline (B1) and

molten states over a pressure and temperature range covering Earth's mantle and conditions in the early magma ocean. We discuss the implications of our results for the composition of the mantle and the origin of the suggested electromagnetic coupling of the core and mantle. In addition, we combine our conductivity results for the molten state of (Mg, Fe)O with our previous results on SiO$_2$ (Scipioni et al., 2017) to examine the conductivity of a magma ocean and its implications for early dynamo action on Earth.

2. Methods

We perform our conductivity calculations on ionic trajectories of (Mg$_{0.75}$, Fe$_{0.25}$)O created by first-principles molecular dynamics simulations using the VASP package (Kresse and Furthmuller, 1996) in the NVT ensemble, as detailed in Holmström and Stixrude (2015, 2016). In these simulations, at a given instant in time, we solve for the electronic charge density of the given ionic configuration within finite-temperature density functional theory (DFT) (Martin, 2008). From the charge density, all physical observables may in principle be computed. The density also allows us to determine the total force acting on each ion, and knowing the instantaneous forces, we propagate Newton's equations of motion forwards for all ions a small time step at a time. In this way, we create trajectories for the ionic and electronic structure of the simulated material at a given volume and temperature, and according to the ergodic hypothesis, time averages of any equilibrium properties that we compute are equal to the ensemble averages and hence thermodynamical averages of these properties. Our periodic simulation cell of solid ferropericlase consists of 64 ions in the B1 structure, whereas the liquid counterpart comprises 128 ions. We sample the Brillouin zone at the Baldereschi point for a lattice of simple cubic symmetry (Baldereschi, 1973) and use a cutoff-energy of 500 eV for the plane-wave basis used to expand the Kohn–Sham electronic orbitals. Exchange and correlation is approximated using the PBEsol (Perdew et al., 2008) functional augmented by the $+U$ methodology (Dudarev et al., 1998) to approximate the strong correlation between the Fe 3d electrons not fully captured by PBEsol. We choose $U - J = 2.5$ eV, which yields agreement with the spin transition pressure seen experimentally (Goncharov et al., 2006). Further details of our molecular dynamics simulations are given in our previous publications (Holmström and Stixrude, 2015, 2016).

We employ the Kubo–Greenwood method to compute the electronic part of the electrical conductivity (σ_{el}) in the crystal and the melt. In the single-particle, DFT implementation of this method (Desjarlais et al., 2002), the optical conductivity at electric field frequency ω for a given point k in the Brillouin zone for a given ionic configuration is

$$\sigma_{el,k}(\omega) = \frac{2\pi e^2 \hbar^2}{3m^2 \omega \Omega} \sum_{i,j=1}^{n} \sum_{\alpha=1}^{3} [F(\epsilon_{i,k}) - F(\epsilon_{j,k})] \tag{1}$$
$$\times |\langle \psi_{j,k} | \nabla_\alpha | \psi_{i,k} \rangle|^2 \delta(\epsilon_{j,k} - \epsilon_{i,k} - \hbar\omega),$$

where $|\psi\rangle_{i,k}$ is the orbital of band number i with wave vector k, the corresponding single-particle eigenvalue being $\epsilon_{i,k}$. The index n denotes the total number of electronic bands, α denotes the Cartesian component, Ω is the volume of the supercell, e is the elementary charge, m is the mass of the electron, and $F(\epsilon)$ is the Fermi–Dirac distribution. The sums thus run over all pairs of orbitals i, j as well as all three spatial directions, where we assume an isotropic medium and a diagonal conductivity tensor. The Kubo–Greenwood method in DFT has been shown to give results in good agreement with experiment for solid (Alfe et al., 2012) and liquid (Desjarlais et al., 2002; Pozzo et al., 2011; Scipioni et al., 2017) metals and semi-metals.

To compute $\sigma_{el}(\omega)$ for a given phase at a given pressure and temperature, we first choose 10 snapshots from the equilibrated MD trajectory in question, the snapshots being sufficiently separated in time to be uncorrelated. Next, for each ionic configuration, we average $\sigma_{el,k}(\omega)$ of Eq. (1) over the Brillouin zone using standard methods (Monkhorst and Pack, 1976). Then, we average the obtained conductivities for the 10 ionic configurations into $\sigma_{el}(\omega)$. Finally, to find the direct-current (DC) conductivity, we determine $\sigma_{el} \equiv \lim_{\omega \to 0} \sigma_{el}(\omega)$. For simplicity and consistency throughout our analysis, we use a standard deviation for the Gaussian representing the δ-function large enough to permit us to simply determine the zero-frequency limit of the conductivity from $\sigma_{el}(\omega)$ at an energy of 1 meV ($\epsilon = \hbar\omega$), thus averting the spurious decay of $\sigma_{el}(\omega)$ at low frequencies (Pozzo et al., 2011).

The low-frequency part and hence the DC limit of the optical conductivity is known to be sensitive to the Brillouin zone sampling as well as the number of ions in the supercell (Pozzo et al., 2011; Alfe et al., 2012). To ensure that our computations are reasonably well converged with respect to these two parameters, we performed test calculations on a single snapshot of the solid trajectory at 3000 K and 94 GPa with all Fe in the low-spin state, and on a single snapshot of the liquid trajectory at 8000 K and 114 GPa, with likewise all Fe in the low-spin state, varying the number of k-points used to sample the Brillouin zone as well as the number of ions for each case. We sampled reciprocal space using no symmetry reduction for the k-point grid (except the time-reversal symmetry of k and $-k$), and as another approach, we sampled the irreducible wedge of the first Brillouin zone assuming perfect cubic symmetry for our supercell. Using 64 ions for the crystal and 128 ions for the melt, we find for both phases that using the irreducible wedge of the lattice of cubic symmetry leads to faster convergence of σ_{el} with respect to the number of k-points than using no symmetry reduction does, but that in the former case, the conductivity converges to a value that is ∼10% off that in the latter approach. We therefore perform our k-point sampling using no symmetry reduction, and find that using 14 k-points (a $3 \times 3 \times 3$ Monkhorst–Pack grid) leads to σ_{el} converged to within 3%. Comparison of the conductivity obtained for the crystalline supercell of 64 ions with that obtained using 216 or 512 atoms indicates that the 64-ion cell gives conductivities to within ∼20% of the values given by the larger supercells. For the melt, we find the 128-ion cell to give conductivities to within ∼10% of those obtained using the larger cells. Overall, using an irreducible $3 \times 3 \times 3$ grid of k-points and 64 ions to represent the crystal and 128 ions to represent the melt, we expect to obtain reasonably well converged DC conductivities for the two phases. We also checked that our values of σ are well converged with respect to the number of bands; for example, for the liquid at 8000 K, σ varies by less than 1% on increasing the number of bands from 595 to 2000.

The equilibrium high-spin fraction $f_{eq}(P, T)$ varies smoothly with pressure and temperature for solid and liquid (Mg, Fe)O (Holmström and Stixrude, 2015, 2016), and our aim is to predict σ_{el} at the equilibrium value of f for each pressure and temperature. We showed in our previous publications how to compute $f_{eq}(P, T)$ by combining constrained-moment and free moment MD simulations, the former producing a low-spin ($f = 0$) and a high-spin ($f = 1$) state and the latter producing two mixed-spin states along each isotherm. We compute the electrical conductivity along each of these MD trajectories, and then determined the value of the conductivity at the equilibrium value f_{eq} by interpolation (see below).

In the liquid phase, the electrical conductivity is determined not solely through the electronic part, but as a sum of σ_{el} and σ_{ion}, where the latter is the total ionic conductivity obtained as a sum over all mobile ionic species. To compute σ_{ion}, we employ the Nernst–Einstein relation (Mookherjee et al., 2008)

$$\sigma_{ion} = \frac{DQ^2 n}{k_B T H_R}, \qquad (2)$$

where D is the total diffusion coefficient not discriminating between ion type, Q is the charge of each ion (we use the formal charge of 2 here for all ion types), n is the ionic number density, and k_B and T are the Boltzmann constant and temperature, respectively. The Haven ratio H_R approaches 1.0 in the dilute limit, and for simplicity, this is the value of H_R we assume.

Finally, as the temperatures in our simulations are much higher than the Néel temperature of crystalline $(Mg_{0.75}, Fe_{0.25})O$, the magnetic moments of the Fe ions in both the solid and liquid phase are expected to be fully disordered, setting the system into a paramagnetic state. The random ordering of the directions of local moments is known to create an additional source of electrical resistivity beyond the usual lattice resistivity due to the thermal perturbation of the crystal structure (ρ_L). This spin-disorder resistivity (ρ_{SD}) (Wysocki et al., 2009) arises in a simple picture from the scattering of itinerant $4s$ electrons by the inhomogeneous exchange potential set up by the $3d$ electrons of the disordered moments. Experimental determination of ρ_{SD} as a function of temperature in a number of ferromagnetic and anti-ferromagnetic metals finds the quantity to plateau to a constant value beyond the Curie or Néel temperature, as expected (Wysocki et al., 2009).

In our DFT calculations, we adopt the collinear approach to treating electron spin, which results in moments or atomic spins in either the "up" or "down" orientation with respect to a global quantization axis. This means that ρ_{SD} is largely missing in our computations, as evinced by test computations of σ_{el} on a supercell of the $(Mg, Fe)O$ crystal where all Fe were in the high-spin state and the collinear moments were either fully ordered or set randomly, the result being a negligible difference in conductivity between the two cases. While no determination of ρ_{SD} and hence no comparison of ρ_{SD} and ρ_L for transition-metal oxides is available in the literature, we perform the following deduction to estimate whether ρ_{SD} is a significant component of the total resistivity $\rho_T = \rho_L + \rho_{SD}$ of $(Mg_{0.75}, Fe_{0.25})O$. For pure Fe, both experiment and non-collinear DFT calculations (Wysocki et al., 2009) find $\rho_{SD}^{Fe} \approx 10^{-6}$ Ωm. The Fe moment in pure Fe ($2S = 2.2\ \mu_B$) is lower than in $(Mg, Fe)O$ ($2S = 3.6\ \mu_B$) in DFT, and if we take $\rho_{SD} \propto S(S+1)$, we find $\rho_{SD}^{(Mg, Fe)O}/\rho_{SD}^{Fe} \approx 2$. However, the concentration of Fe and hence magnetic moments is diluted in $(Mg_{0.75}, Fe_{0.25})O$ with respect to pure Fe, and we thus take $\rho_{SD}^{(Mg, Fe)O} \approx \rho_{SD}^{Fe} = 10^{-6}$ Ωm as a first-order estimate. This estimate is 1–2 orders of magnitude smaller than the total electrical resistivity of our calculations meaning that spin-disorder resistivity may be safely neglected when determining the total electrical conductivity of the material.

To compute the electronic component of the thermal conductivity (κ_{el}), we use the Chester–Thellung formulation of the Kubo–Greenwood method, which states that

$$\kappa_{el,k}(\omega) = \frac{1}{e^2 T}\left(L_{22}(\omega) - \frac{L_{12}(\omega)^2}{\sigma(\omega)} \right), \qquad (3)$$

where the kinetic coefficients $L_{ij}(\omega)$ are defined as

$$
\begin{aligned}
L_{k,lm}(\omega) = (-1)^{l+m} \frac{2\pi e^2 \hbar^2}{3m^2 \omega \Omega} \sum_{i,j=1}^{n} \sum_{\alpha=1}^{3} [F(\epsilon_{i,k}) - F(\epsilon_{j,k})] \\
\times |\langle \psi_{j,k} | \nabla_\alpha | \psi_{i,k} \rangle|^2 [\epsilon_{j,k} - \mu]^{l-1} [\epsilon_{i,k} - \mu]^{m-1} \\
\times \delta(\epsilon_{j,k} - \epsilon_{i,k} - \hbar\omega),
\end{aligned}
\qquad (4)
$$

where μ is the electron chemical potential (Pozzo et al., 2011). Using the same procedure as for the electrical conductivity, we average the thermal conductivity over the Brillouin zone and over
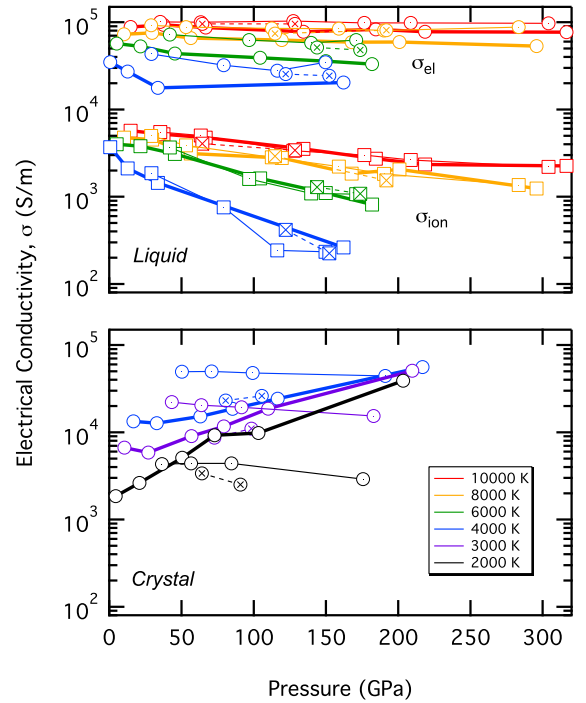

Fig. 1. Electrical conductivity of liquid (top) and crystal (bottom) as a function of pressure at various temperatures color-coded according to the legend. The electronic component (circles) and (for the liquid) the ionic component (squares) are shown. At each temperature, three curves are shown: bold line and plain symbols for high-spin, narrow line and dotted symbols for low-spin and dashed line and crossed symbols for mixed spin results. (For interpretation of the colors in the figure(s), the reader is referred to the web version of this article.)

10 uncorrelated ionic configurations, and take the zero-frequency limit to find $\kappa_{el} = \lim_{\omega \to 0} \kappa_{el}(\omega)$.

3. Results

3.1. Electrical conductivity

We present σ_{el} for the $(Mg, Fe)O$ crystal and liquid in Fig. 1. In addition to an anticipated dependency of σ_{el} on pressure and temperature, the conductivity is clearly dependent also on the high-spin fraction f. In the crystal, σ_{el} increases with compression in the high spin state, and decreases on compression for the low spin state. In the liquid, σ_{el} decreases with compression. The variation of σ_{el} with f is non-linear, and, for the two lowest temperatures considered ($T = 2000, 3000$ K), the conductivity of the crystal is somewhat lower at intermediate f than at $f = 0.0$ or $f = 1.0$.

For the liquid, we also report the ionic component of the electrical conductivity in Fig. 1. This contribution to the conductivity is small and becomes smaller with increasing pressure, as diffusivity is diminished, the decrease in diffusivity thus dominating over the simultaneous increase in ionic density (Eq. (2)). Ionic conductivity increases with increasing temperature, as expected from the well-known Arrhenius relation $D \propto \exp(-H/k_B T)$, where H is the activation enthalpy of diffusion (Holmström and Stixrude, 2016). Overall, σ_{ion} is approximately an order of magnitude smaller than σ_{el}.

3.2. Thermal conductivity

We present the electronic component of the thermal conductivity of the crystal and the liquid in Fig. 2. The similarity of pressure and temperature dependence of κ_{el} to that of σ_{el} is apparent for each phase. We find that although neither the crystal
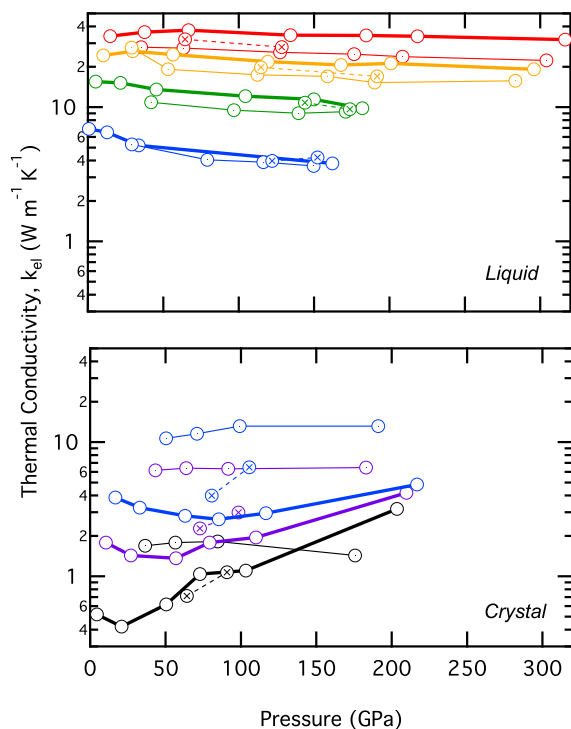
Fig. 2. Electronic component of the thermal conductivity of liquid (top) and crystal (bottom) as a function of pressure at various temperatures color-coded according to the legend in Fig. 1. At each temperature, three curves are shown: bold line and plain symbols for high-spin, narrow line and dotted symbols for low-spin and dashed line and crossed symbols for mixed spin results.

Fig. 3. Electronic density of states of the crystal for $f = 1$ ($P = 21$ GPa, $T = 2000$ K) (top), $f = 0$ ($P = 191$ GPa, $T = 4000$ K) (middle) and liquid for $f = 1$ ($P = 1$ GPa, $T = 4000$ K). Arrows indicate trends with increasing pressure: lifting of the Jahn–Teller-like pseudogap in the HS crystal, increased t_{2g}–e_g splitting in the LS crystal, and increased band broadening in the liquid.

nor the liquid is a good metal at the conditions explored here, the electronic components of κ and σ in both phases approximately obey the empirical law of Wiedemann and Franz, $\kappa = L\sigma T$, where L is the Lorenz number (Ashcroft and Mermin, 1976). We find $L = (6 \pm 3) \times 10^{-8}$ and $(1.3 \pm 0.7) \times 10^{-7}$ WΩ/K^2 for the crystal at $f = 1.0$ and 0.0, respectively, where the error is the standard deviation over the explicitly simulated conditions. For the liquid, we find $L = (4.7 \pm 0.7) \times 10^{-8}$ and $(2.7 \pm 0.4) \times 10^{-8}$ WΩ/K^2 for $f = 1.0$ and 0.0, respectively, closer to the theoretically derived value of $L = 2.4 \times 10^{-8}$ WΩ/K^2.

3.3. Electronic density of states

The variation of conductivity with pressure and temperature can be understood by examining the electronic density of states (Fig. 3). The system is semi-metallic at all conditions that we have studied in crystal and liquid phases: the density of states at the Fermi level is non-zero, but is significantly less than expected of an ordrinary metal (Ashcroft and Mermin, 1976). The situation at the conditions of our simulations therefore differs from that near room temperature where ferropericlase is known to be insulating, with optical properties in excellent agreement with our static calculations (Holmström and Stixrude, 2015). Increasing temperature causes the gap to close converting the gap to a pseudogap with a finite density of states at the Fermi level $N(E_F)$.

Variations of σ with pressure and temperature track those of $N(E_F)$. Consider first the low spin crystal. The mostly occupied t_{2g} states and the mostly unoccupied e_g states overlap slightly, producing a finite $N(E_F)$. With increasing pressure, the t_{2g}–e_g splitting grows, reducing the overlap and thus reducing $N(E_F)$ and explaining the pressure-induced decrease in σ (Fig. 1). In the liquid, t_{2g} and e_g states are not distinguished because octahedra are not aligned with the global coordinate axes, and there are many non-octahedral coordination environments. The d-band
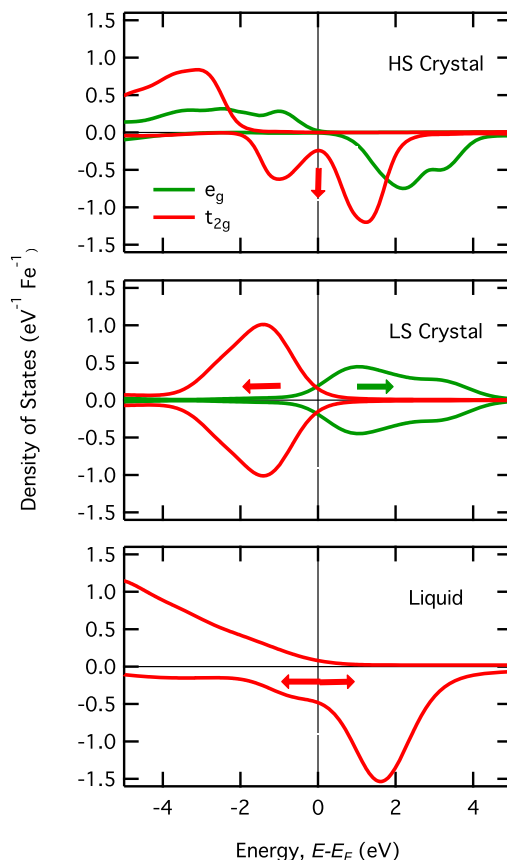
in both high spin and low spin channels broadens with increasing pressure, thus reducing $N(E_F)$ and accounting for the pressure induced decrease in σ. In the high spin crystal, the Fermi level falls at a pseudo-gap within the minority-spin t_{2g} band, caused by Jahn–Teller distortion. With increasing pressure, this distortion diminishes, lifting the pseudo-gap and causing $N(E_F)$ to increase, explaining the pressure-induced increase in σ. Spectroscopic data on ferropericlase also show evidence of Jahn–Teller distortion at low pressure and the quenching of this distortion as pressure increases (Keppler et al., 2007).

3.4. Electrical and thermal conductivity in equilibrium

Ferropericlase undergoes a broad pressure-induced high spin to low spin crossover. We have previously shown how to compute the equilibrium spin fraction $f_{eq}(P, T)$ at any pressure and temperature from first principles molecular dynamics (Holmström and Stixrude, 2015, 2016). We combine these results with those presented above to obtain the variation of the electrical and thermal conductivity at $f_{eq}(P, T)$ (Fig. 4). We assume linear interpolation in $\log\sigma$-pressure space, and quadratic in f, according to

$$\sigma^{-1}(P, T, f_{eq}) = f_{eq}\sigma^{-1}(P, T, 1) + (1 - f_{eq})\sigma^{-1}(P, T, 0)$$
$$+ C_f(T)f_{eq}(1 - f_{eq}) \qquad (5)$$

and we determine the value of C_f along each isotherm by fitting to our ab initio results (Figs. 1, 2), finding that the value of C_f is independent of pressure to within our resolution. The quadratic
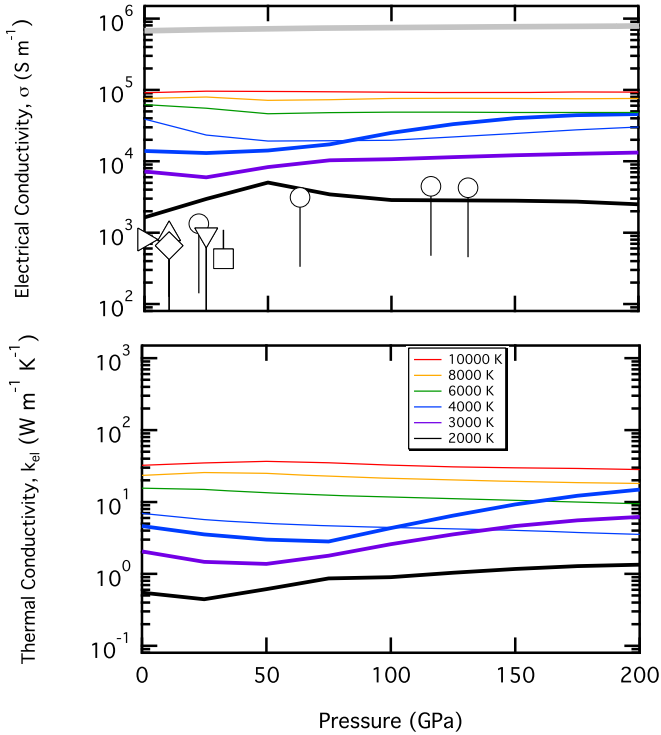
Fig. 4. Electrical conductivity (top) and electronic component of thermal conductivity (bottom) vs. pressure for crystal (bold lines) and liquid (narrow lines) with color indicating temperature according to the legend. The liquid values shown in the top panel are the total conductivity: $\sigma = \sigma_{el} + \sigma_{ion}$. Symbols indicate experimental measurements of the electrical conductivity of (Mg,Fe)O: Wood and Nell (1991): ▷; Dobson and Brodholt (2000): △; Xu et al. (2000): ◇; Ohta et al. (2017): ○; Yoshino et al. (2008): ▽; Li and Jeanloz (1990): □. Symbols are plotted at the value corresponding to $X_{Fe} = 0.25$ and $T = 2000$ K; vertical lines connect the symbols to the value of X_{Fe} measured. We also compare to the minimum metallic conductivity of Mott (1972) (grey band).

dependence on f follows Nordheim's rule for the positive contribution of disorder to resistivity, in this case reflecting the influence of high-spin / low-spin configurational disorder over the Fe lattice sites (Ashcroft and Mermin, 1976).

The behavior of σ_{el} of the crystal at 2000 K shows the influence of the high-spin to low-spin crossover. The conductivity increases with pressure initially and then near the onset of the cross-over at 50 GPa, it decreases, before assuming a nearly constant value at higher pressure. This behavior reflects that seen experimentally at 300 K where the high-spin to low-spin crossover causes a sigmoidal variation in σ_{el} with increasing pressure (Ohta et al., 2007). The effect of the crossover is less prominent at high temperature because the spin crossover takes place over a broader range of pressure and because peaks in the electronic density of states that underly the different behavior of high spin and low spin states are more washed out. In the liquid, the variation of $\log \sigma$ with pressure is nearly linear, except at the lowest temperature explored.

Our results are in reasonably good agreement with previous experimental data (Fig. 4). In order to compare with previous results, all of which have been performed at different iron concentrations $X_{Fe} = Fe/(Fe + Mg)$, we must correct for the influence of X_{Fe} on σ_{el}. Previous experiments (Li and Jeanloz, 1990) show this dependence to be very strong, approximating

$$\log_{10} \sigma (X_{Fe}) = \log_{10} \sigma (0.25) + 16(X_{Fe} - 0.25) \qquad (6)$$

which we have assumed in correcting all experimental data to $X_{Fe} = 0.25$. We have also interpolated or extrapolated experimental measurements to 2000 K, using the temperature dependence

recommended in the respective experimental study. At low pressure ($P < 50$ GPa), our results are a factor of 2–3 (0.3–0.5 log units) larger than experiment, (except for the result of Li and Jeanloz, 1990 which appears to be significantly smaller than other experimental values). Possible reasons for this discrepancy include scattering from Fe–Mg disorder. In our calculations, we have assumed a perfectly ordered arrangement of Mg and Fe atoms. It is known that chemical disorder can have a large influence on σ_{el}. For example, Cu_3Au at ambient conditions is 2.5 times more conductive in the ordered state as compared with the disordered state (Johansson and Linde, 1936), a difference that is very similar to what we find between our ordered ab initio results and (presumably) disordered experimental data. On the other hand, our calculations do not *uniformly* overestimate experimental values. At $P > 100$ GPa, the experimental conductivity is slightly larger than the ab initio results. It is possible that the effect of disorder is diminished in the low spin state because low spin iron has a very similar cation radius to Mg. It is also possible that the effect of iron on the conductivity at high pressure is considerably weaker than that assumed here (Eq. (6)), which is based on experimental data that comes entirely from the high spin state.

No experimental measurements of the conductivity of oxide or silicate liquids are available at the conditions of our simulations. Near ambient pressure and at temperature near freezing, electrical conductivity is small ($\sigma < 100$ S/m), and ions are the dominant charge carriers (Ni et al., 2015). Our high pressure, temperature results are in a different regime in which electrons are the dominant charge carriers (Fig. 1). Experimental observations of significant optical reflectivity in geophysically relevant liquids support our findings (McWilliams et al., 2012). The electrical conductivity may be estimated from the optical measurements and are found to be in a range similar to our results, for example in MgO (10^4 S/m) (McWilliams et al., 2012) at somewhat higher pressure and temperature conditions.

4. Discussion

4.1. Conduction mechanisms in crystal and liquid

We find that σ increases with increasing temperature. It has been claimed that an increase of σ on heating means that the system must be semi-conducting with a finite gap (Ohta et al., 2017), in contrast to our system, which has no gap. While it is true that in ordinary metals σ decreases on heating due to phonon scattering, in our system, there is a far more important barrier to conduction that renders phonon scattering relatively unimportant: the low value of the density of states at the Fermi level $N(E_F)$. The density of states at the Fermi level grows with increasing temperature, and this temperature-induced increase in $N(E_F)$ controls the increase in σ with increasing temperature, swamping the effects of phonon scattering. At low pressure, the conductivity continues to increase through the melting transition. At high pressure, the crystal has a higher value of σ than the liquid at the same temperature.

Experimental measurements show that the dominant conduction mechanism at temperatures $T < 2000$ K, i.e. just below the temperature range of our study, is a small polaron hopping mechanism between Fe^{2+} and Fe^{3+} defects. This mechanism is absent in our calculations because our system is free of ferric iron. We propose on the basis of our results, and the reasonably good agreement that we find with experimental measurements of the conductivity (Fig. 4) that the band conduction mechanism which we find overtakes the small polaron hopping mechanism at a temperature near 2000 K and that the band mechanism dominates at higher temperature. Indeed some experimental data show an

increase in the apparent activation energy as the temperature approaches 2000 K (Ohta et al., 2017), suggesting a transition with increasing temperature from the small polaron mechanism to a new mechanism, which we identify as the band mechanism. We note that the band conduction mechanism is only slightly influenced by the presence of Fe^{3+} defects in proportions likely to exist in the lower mantle, i.e. a few percent. Such defects reduce $N(E_F)$ in linear proportion to the ferric to total iron concentration, i.e. by only a few percent.

4.2. Electrical conductivity of the lower mantle

To find σ of ferropericlase in the lower mantle we linearly interpolate our first principles results (Fig. 4) in $\log \sigma (P, T)$ space and correct for variations in X_{Fe} according to Eq. (6). To explore the full range of X_{Fe} that ferropericlase might have in the lower mantle, we consider two approximations to the ferropericlase-bridgmanite Mg–Fe partition coefficient K. For an Al-free system, representative of a harzburgitic lower mantle component (Stixrude and Lithgow-Bertelloni, 2012), we adopt $K(P, T)$ from Nakajima et al. (2012). For an Al-bearing system, representative of pyrolite, we assume $K = 0.5$, which is consistent within uncertainty with the pressure-variable value of K found in Piet et al. (2016). We assume a bulk iron concentration $X_{Fe} = 0.1$, and ferropericlase volume fraction $F = 0.2$ for both compositional models. We compute the Hashin–Shtrikman bounds and the result of the self-consistent effective medium theory (Berryman, 1995). We interpolate all results onto the geotherm of Stixrude et al. (2009) consisting of the 1600 K isentrope with a lower thermal boundary layer reaching 4000 K at the core-mantle boundary.

The value of σ of ferropericlase in the lower mantle that we find is 3–30 times higher than that according to the Arrhenius relation of Xu et al. (2000), which has been widely used in modeling studies (Püthe et al., 2015) (Fig. 5). The primary reason for this difference is the iron concentration of ferropericlase: whereas (Xu et al., 2000) is based on measurements at $X_{Fe} = 0.11$ and is not corrected for iron concentration, X_{Fe} of ferropericlase at 1000 km depth is significantly greater, lying in the range 0.14–0.18, depending on the bulk composition (ferropericlase is more iron-rich and more conductive in the Al-free system because iron more strongly partitions into ferropericlase in this system). Some more recent modeling studies (Deschamps and Khan, 2016) have corrected for iron concentration according to the scheme of Vacher and Verhoeven (2007), which yields similar results to our Eq. (6). There are other important differences. Whereas Xu et al. (2000) and Deschamps and Khan (2016) assume a constant activation volume, we find that the pressure dependence of $\log \sigma$ is non-linear in pressure, with a weak dependence on pressure after the high spin to low spin transition. Therefore, our results cannot be fit accurately to an Arrhenius form. However, as we recognize the potential value of a simple, approximate representation, we have found a best-fitting Arrhenius relation, which deviates from our ab initio $X_{Fe} = 0.25$ results by no more than 0.3 log-units

$$\sigma \approx \sigma_0 \exp^{-(\Delta E + P \Delta V)/RT} \quad (7)$$

with $\sigma_0 = 1.99 \times 10^5 \ S\,m^{-1}$, $\Delta E = 75.94 \ kJ\,mol^{-1}$, and $\Delta V = -0.061 \ cm^3\,mol^{-1}$. We caution that these are effective fit parameters with limited physical significance. The deviations between this fit and our results is largest in the vicinity of the high-spin to low-spin transition. Values of σ at other value of X_{Fe} may be estimated by combining Eqs. (6)–(7).

A harzburgitic lower mantle matches the geophysical observations much better than a pyrolitic lower mantle (Fig. 5). We note that in both cases, the volumetrically minor and more conductive
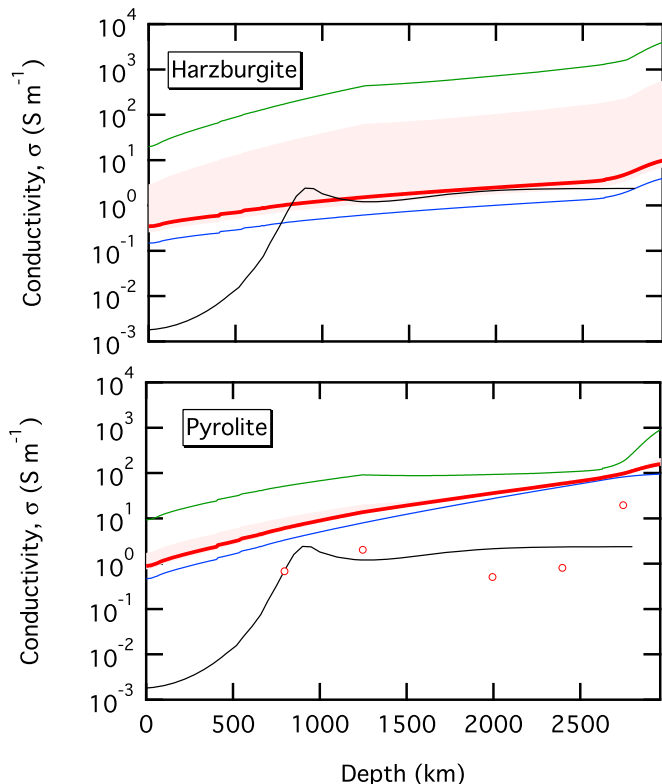

Fig. 5. Electrical conductivity of harzburgite (top) and pyrolite (bottom) lower mantle (bold red lines showing the self-consistent result and shading indicating Hashin–Shtrikman bounds) along the geotherm of Stixrude et al. (2009). Also shown are the conductivities of the two phases: ferropericlase, interpolated from our results as described in the text (green lines) and bridgmanite (blue lines) from Xu et al. (2000) for the Al-free (top) and from Sinmyo et al. (2014) for the Al-bearing (bottom) compositions, experimental measurements of pyrolite (circles) (Ohta et al., 2010), and the geophysically inverted model of Püthe et al. (2015) (black line).

component, ferropericlase, has a small effect on the conductivity of the two-phase assemblage according to the self-consistent theory. Thus, a lower mantle consisting of a mechanical mixture of harzburgite and a much smaller proportion of basalt, would be expected to have a σ profile very similar to our result for harzburgite. The pyrolite σ profile is much higher than the geophysically inverted profile throughout the lower mantle. The reason for this discrepancy is that the conductivity of the Al–Fe bearing bridgmanite phase is much higher than that of the lower mantle. We note that Sinmyo et al. (2014) argued that the very large value of σ of Al–Fe bearing bridgmanite could be reconciled with geophysical observation if ferropericlase had a lower value of σ than that of bridgmanite. However, this picture does not agree with our results: we find σ of ferropericlase to be even higher than that of Al–Fe bearing bridgmanite. The conductivity of Al–Fe bridgmanite found by Sinmyo et al. (2014) apparently disagrees with measurements of pyrolite (Ohta et al., 2010). The pyrolite measurements show much lower values, in good agreement with geophysical observations. The reason for this discrepancy is not clear, although it may be due to slight differences in composition in the two studies that can have a large, though still poorly constrained impact on σ of bridgmanite such as the ferric/ferrous ratio (Yoshino et al., 2016).

Direct comparison to geophysical observation confirms these patterns: a harzburgite-dominated mantle matches the lower mantle better than a pyrolitic mantle (Fig. 6). We note in this context that geophysical inversions of the lower mantle conductivity profile are inherently non-unique, which is why it is important to compare with the observations directly. Even satellite-based ob-
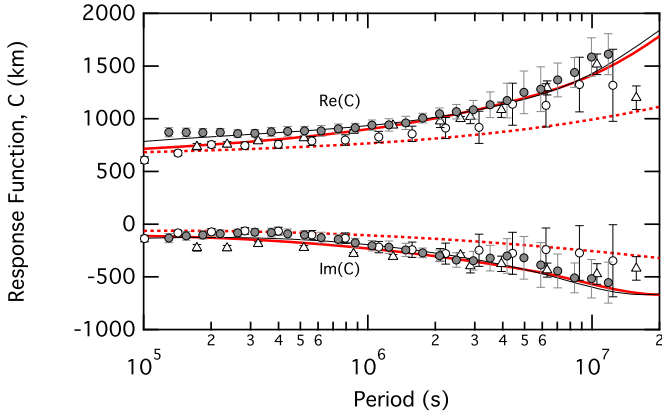
Fig. 6. Observed C-responses from satellite (Püthe et al., 2015 shaded circles; Kuvshinov and Olsen, 2006 open circles) and observatory (Olsen, 1999 triangles) data compared with that of the inversion of Püthe et al. (2015) (black line), and our two compositional models: harzburgite (bold red line) and pyrolite (dashed red line).

servations are subject to uncertainty in the form of corrections for three-dimensional effects, which can vary by an amount similar to or somewhat larger than the reported uncertainty as the comparison between the data of Püthe et al. (2015) and Kuvshinov and Olsen (2006) shows. Moreover, there may be real lateral variations in the deep electrical conductivity profile, which may account for the differences between the satellite based observations and those from European observatories (Olsen, 1999). We compute the C-response of the mantle by adopting the upper mantle portion of the conductivity profile of Püthe et al. (2015) in the range 0–660 km depth and our profile (bold red lines in Fig. 5) in the lower mantle (660–2891 km depth). The mantle is underlain by a perfectly conducting core. We compute the C-response for the H^+ model by applying the flat Earth transform (Weidelt, 1972) and the formalism of Parker (1980) via the recursion relation

$$\tilde{C}_n = h_n P - \frac{h_n}{P + \tilde{C}_{n+1}/d} \tag{8}$$

which we continue until $n = 1$: the surface layer. Here h_n and σ_n are the thickness and conductivity of layer n, respectively, $P = \cosh(d\sqrt{i\omega})$, $d = \sqrt{\mu_0 \sigma_n h_n^2}$ is a constant that sets the layer spacings (we choose $d = 10$ m), μ_0 is the magnetic permeability, ω is the angular frequency, $i = \sqrt{-1}$, and the C-response $C = \tilde{C}/[d\sqrt{i\omega}\sinh(d\sqrt{i\omega})]$.

Our results indicate that electrical conductivity is a sensitive probe of lithologic heterogeneity in the lower mantle. The electrical conductivity of the harzburgite-dominated mechanical mixture is substantially lower than that of the equilibrium pyrolite assemblage, largely due to the presence of significant Al and ferric iron in bridgmanite in pyrolite. Many studies of the elasticity of lower mantle phases have focused on equilibrium assemblages, such as pyrolite, for comparison with lower mantle seismic observations (Zhang et al., 2016). We suggest that in future such studies also consider lithologically heterogeneous assemblages, such as those proposed by Stixrude and Lithgow-Bertelloni (2012).

4.3. Electrical conductivity of ULVZ

Evidence from studies of nutations indicates that there may be a highly electrically conductive layer at the core-mantle boundary (Buffett, 1992). It is possible that this layer also explains the origin of ultra low velocity zones (ULVZ) (Buffett et al., 2000). Here, we explore this hypothesis further by examining an end-member scenario in which ULVZ are composed entirely of $(Mg_{0.75}Fe_{0.25})O$ fer-

ropericlase. An attractive feature of this model is that the electrical conductivity is very high. We find $\sigma = 3.6 \times 10^4$ S m^{-1} at 136 GPa and 4000 K (Fig. 4). Nutations require a conductance over the putative high conductivity layer of 10^8 S, which, in combination with our value for σ, implies a thickness of 3 km, somewhat smaller than the inferred thickness of ULVZ from seismology. Moreover, the seismic properties of $(Mg_{0.75}Fe_{0.25})O$ ferropericlase agree reasonably well with those of the ULVZ: the P-wave velocity anomaly agrees perfectly, while a slightly more iron-rich composition is preferred to explain the S-wave anomaly (Muir and Brodholt, 2015). On the other hand, ferropericlase alone cannot also explain the seismically constrained density anomaly, although this is perhaps the least well constrained property of ULVZ from seismology (Muir and Brodholt, 2015). Some admixture of bridgmanite with Fe-rich ferropericlase may explain the seismological observations better (Muir and Brodholt, 2015). Moreover, addition of bridgmanite lowers σ allowing a thicker layer to explain the nutation-constrained conductance in better agreement with seismic estimates of ULVZ thickness.

A potential difficulty with this picture is that a mixture of iron-rich ferropericlase and bridgmanite may be partially or completely molten at conditions of the core-mantle boundary. The relevant melting relations are poorly constrained. However, it is known that the pressure–temperature conditions at the core-mantle boundary coincide with the pyrolite solidus (Fiquet et al., 2010), that bridgmanite is the liquidus phase in a pyrolite bulk composition (Fiquet et al., 2010), and that iron enrichment lowers the melting temperature over a wide pressure interval (Du and Lee, 2014). It has been suggested that a partial melt may also be a viable explanation for the observed properties of ULVZ (Williams and Garnero, 1996; Stixrude et al., 2009). Our results show that a liquid of $(Mg_{0.75}Fe_{0.25})O$ composition has a somewhat lower σ than the crystal: $\sigma = 2.3 \times 10^4$ S m^{-1} for the liquid at 136 GPa and 4000 K (Fig. 4). Addition of crystalline bridgmanite or crystalline ferropericlase with X_{Fe} less than that of the liquid phase further lowers the conductivity allowing for high conductance layers with thickness greater than 3 km.

4.4. Electrical conductivity of the basal magma ocean

An initially molten Earth, crystallizing from the mid-mantle, may have sustained a basal magma ocean for a billion years (Labrosse et al., 2007). Could this basal magma ocean have produced a magnetic field? If so, it may help to explain the existence of the early terrestrial magnetic field at a time when heat flow from the core is thought to have been far less than that required to sustain a core dynamo. The crucial requirement is that the electrical conductivity of the magma ocean be sufficiently large (Ziegler and Stegman, 2013). We have recently found that pure silica liquid has an electrical conductivity at basal magma ocean conditions sufficient to sustain a dynamo (Scipioni et al., 2017). Our present results strengthen this conclusion by showing that $(Mg, Fe)O$, as another major component of the magma ocean, has a value of σ 19 times larger than that of SiO_2 liquid at 136 GPa and 4000 K (Fig. 7). We conclude that σ of the basal magma ocean was almost certainly higher than that of pure silica and far in excess of the minimum required to sustain a dynamo. Calculations based on an estimated liquid crystal partition coefficient show that the basal magma ocean may reach $X_{Fe} = 0.25$ at 80% crystallization (Zhang et al., 2016). More detailed estimates of the conductivity of the magma ocean are not possible at this time for at least two reasons: 1) the evolution of the Mg/Si ratio of the basal magma ocean as a function of fractional crystallization and 2) the variation of the electrical conductivity with Mg/Fe and Mg/Si ratios are unknown.
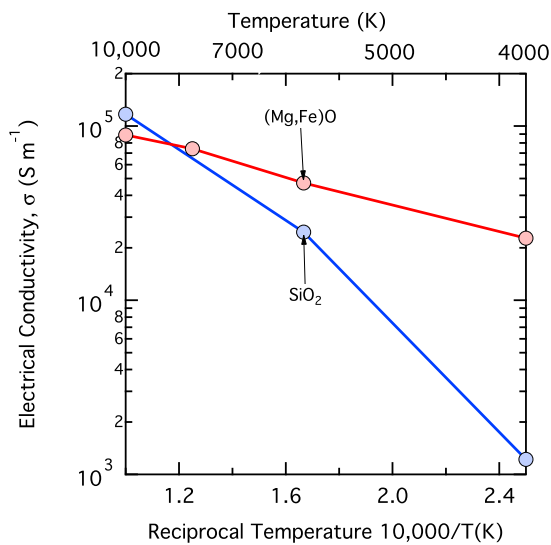
Fig. 7. Electrical conductivity of $(Mg_{0.75}Fe_{0.25})O$ (red, present study) and SiO_2 (blue, Scipioni et al., 2017) liquid as a function of temperature at 136 GPa.

4.5. Electronic contribution to thermal conductivity

We find the electronic contribution to thermal conductivity at the core-mantle boundary to be negligible. Our results yield $k_{el} = 8.57$ W/m/K at 136 GPa and 4000 K (Fig. 4). As our results approximately satisfy the Wiedemann–Franz relation, we assume that we may correct k_{el} for X_{Fe} according to Eq. (6). For the harzburgitic model, which produces the more iron-rich ferropericlase and thus the largest value of k_{el}, we have $X_{Fe} = 0.19$, and therefore $k_{el} = 0.8$ W/m/K. This is a small fraction of the lattice thermal conductivity of ferropericlase at the core-mantle boundary: 20 ± 5 W/m/K for pure MgO (Stackhouse et al., 2010) and 15.8 W/m/K, after accounting for the effects of Fe substitution (Stackhouse et al., 2015). Thus the electronic contribution is only 5% of the lattice contribution and smaller than the uncertainties in the lattice contribution. These conclusions are in excellent agreement with those of Ohta et al. (2017).

5. Conclusions

Using density functional theory, we compute the electronic component of the electrical and thermal conductivity of the $(Mg, Fe)O$ crystal and liquid over a broad range of planetary conditions. Both phases are semi-metallic at mantle conditions of pressure, temperature and iron concentration. Our results are consistent with geophysical determinations of the electrical conductivity of Earth's mantle when combined with values of the conductivity of Al-poor perovskite, and thus a mechanical mixture of dominantly harzburgite with secondary basalt (Stixrude and Lithgow-Bertelloni, 2012). Laboratory measurements on the electrical conductivity of $(Mg, Fe)O$ agree reasonably well with our simulations (to within 0.2–0.5 log units) when corrected to the same iron concentration, with the remaining discrepancy likely accounted for by lattice disorder. The high conductivity at the bottom of the mantle allowed by our calculations can be used to explain the electromagnetic coupling of the core and mantle inferred from length-of-day observations. The electrical conductivity of a basal magma ocean is sufficient to sustain a silicate dynamo.

Acknowledgements

References

Alfe, D., Pozzo, M., Desjarlais, M.P., 2012. Lattice electrical resistivity of magnetic bcc iron from first-principles calculations. Phys. Rev. B 85, 024102.

Ashcroft, N.W., Mermin, N.D., 1976. Solid State Physics. Holt Rinehart and Winston, New York.

Baldereschi, A., 1973. Mean-value point in Brillouin zone. Phys. Rev. B 7, 5212–5215.

Berryman, J.G., 1995. Mixture theories for rock properties. In: Ahrens, T.J. (Ed.), Rock Physics and Phase Relations: A Handbook of Physical Constants. American Geophysical Union, Washington, DC, pp. 205–228.

Buffett, B.A., 1992. Constraints on magnetic energy and mantle conductivity from the forced nutations of the Earth. J. Geophys. Res., Solid Earth 97, 19581–19597.

Buffett, B.A., Garnero, E.J., Jeanloz, R., 2000. Sediments at the top of Earth's core. Science 290, 1338–1342.

Deschamps, F., Khan, A., 2016. Electrical conductivity as a constraint on lower mantle thermo-chemical structure. Earth Planet. Sci. Lett. 450, 108–119.

Desjarlais, M.P., Kress, J.D., Collins, L.A., 2002. Electrical conductivity for warm, dense aluminum plasmas and liquids. Phys. Rev. E 66, 025401.

Dobson, D.P., Brodholt, J.P., 2000. The electrical conductivity of the lower mantle phase magnesiowustite at high temperatures and pressures. J. Geophys. Res., Solid Earth 105, 531–538.

Du, Z.X., Lee, K.K.M., 2014. High-pressure melting of MgO from (Mg, Fe)O solid solutions. Geophys. Res. Lett. 41, 8061–8066.

Dudarev, S.L., Botton, G.A., Savrasov, S.Y., Humphreys, C.J., Sutton, A.P., 1998. Electron-energy-loss spectra and the structural stability of nickel oxide: an LSDA+U study. Phys. Rev. B 57, 1505–1509.

Fiquet, G., Auzende, A.L., Siebert, J., Corgne, A., Bureau, H., Ozawa, H., Garbarino, G., 2010. Melting of peridotite to 140 gigapascals. Science 329, 1516–1518.

Goncharov, A.F., Struzhkin, V.V., Jacobsen, S.D., 2006. Reduced radiative conductivity of low-spin (Mg, Fe)O in the lower mantle. Science 312, 1205–1208.

Holmström, E., Stixrude, L., 2015. Spin crossover in ferropericlase from first-principles molecular dynamics. Phys. Rev. Lett. 114, 117202.

Holmström, E., Stixrude, L., 2016. Spin crossover in liquid (Mg, Fe)O at extreme conditions. Phys. Rev. B 93, 195142.

Johansson, C.H., Linde, J.O., 1936. Röntgenographische und elektrische untersuchungen des CuAu-Systems. Ann. Phys. 25, 1–48.

Keppler, H., Kantor, I., Dubrovinsky, L.S., 2007. Optical absorption spectra of ferropericlase to 84 GPa. Am. Mineral. 92, 433–436.

Kresse, G., Furthmuller, J., 1996. Efficient iterative schemes for ab initio total-energy calculations using a plane-wave basis set. Phys. Rev. B 54, 11169–11186.

Kuvshinov, A., Olsen, N., 2006. A global model of mantle conductivity derived from 5 years of CHAMP, orsted, and SAC-C magnetic data. Geophys. Res. Lett. 33, L18301.

Labrosse, S., Hernlund, J.W., Coltice, N., 2007. A crystallizing dense magma ocean at the base of the Earth's mantle. Nature 450, 866–869.

Li, X.Y., Jeanloz, R., 1990. High pressure–temperature electrical-conductivity of magnesiowustite as a function of iron-oxide concentration. J. Geophys. Res. B, Solid Earth Planets 95, 21609–21612.

Martin, R.M., 2008. Electronic Structure: Basic Theory and Practical Methods. Cambridge University Press, Cambridge.

McWilliams, R.S., Spaulding, D.K., Eggert, J.H., Celliers, P.M., Hicks, D.G., Smith, R.F., Collins, G.W., Jeanloz, R., 2012. Phase transformations and metallization of magnesium oxide at high pressure and temperature. Science 338, 1330–1333.

Monkhorst, H.J., Pack, J.D., 1976. Special points for Brillouin-zone integrations. Phys. Rev. B 13, 5188–5192.

Mookherjee, M., Stixrude, L., Karki, B., 2008. Hydrous silicate melt at high pressure. Nature 452, 983–986.

Mott, N.F., 1972. Conduction in non-crystalline systems 9. Minimum metallic conductivity. Philos. Mag. 26, 1015–1026.

Muir, J.M.R., Brodholt, J.P., 2015. Elastic properties of ferropericlase at lower mantle conditions and its relevance to ULVZs. Earth Planet. Sci. Lett. 417, 40–48.

Nakajima, Y., Frost, D.J., Rubie, D.C., 2012. Ferrous iron partitioning between magnesium silicate perovskite and ferropericlase and the composition of perovskite in the Earth's lower mantle. J. Geophys. Res., Solid Earth 117, B08201.

Ni, H.W., Hui, H.J., Steinle-Neumann, G., 2015. Transport properties of silicate melts. Rev. Geophys. 53, 715–744.

Ohta, K., Hirose, K., Ichiki, M., Shimizu, K., Sata, N., Ohishi, Y., 2010. Electrical conductivities of pyrolitic mantle and MORB materials up to the lowermost mantle conditions. Earth Planet. Sci. Lett. 289, 497–502.

Ohta, K., Hirose, K., Onoda, S., Shimizu, K., 2007. The effect of iron spin transition on electrical conductivity of (Mg, Fe)O magnesiowustite. Proc. Jpn. Acad. Ser. B, Phys. Biol. Sci. 83, 97–100.

Ohta, K., Yagi, T., Hirose, K., Ohishi, Y., 2017. Thermal conductivity of ferropericlase in the Earth's lower mantle. Earth Planet. Sci. Lett. 465, 29–37.

Olsen, N., 1999. Long-period (30 days–1 year) electromagnetic sounding and the electrical conductivity of the lower mantle beneath Europe. Geophys. J. Int. 138, 179–187.

Parker, R.L., 1980. The inverse problem of electromagnetic induction – existence and construction of solutions based on incomplete data. J. Geophys. Res. 85, 4421–4428.

Perdew, J.P., Ruzsinszky, A., Csonka, G.I., Vydrov, O.A., Scuseria, G.E., Constantin, L.A., Zhou, X.L., Burke, K., 2008. Restoring the density-gradient expansion for exchange in solids and surfaces. Phys. Rev. Lett. 100, 136406.

Piet, H., Badro, J., Nabiei, F., Dennenwaldt, T., Shim, S.H., Cantoni, M., Hebert, C., Gillet, P., 2016. Spin and valence dependence of iron partitioning in Earth's deep mantle. Proc. Natl. Acad. Sci. USA 113, 11127–11130.

Pozzo, M., Desjarlais, M.P., Alfe, D., 2011. Electrical and thermal conductivity of liquid sodium from first-principles calculations. Phys. Rev. B 84, 054203.

Püthe, C., Kuvshinov, A., Khan, A., Olsen, N., 2015. A new model of Earth's radial conductivity structure derived from over 10 yr of satellite and observatory magnetic data. Geophys. J. Int. 203, 1864–1872.

Scipioni, R., Stixrude, L., Desjarlais, M.P., 2017. Electrical conductivity of SiO_2 at extreme conditions and planetary dynamos. Proc. Natl. Acad. Sci. USA 114 (34), 9009–9013.

Sinmyo, R., Pesce, G., Greenberg, E., McCammon, C., Dubrovinsky, L., 2014. Lower mantle electrical conductivity based on measurements of Al, Fe-bearing perovskite under lower mantle conditions. Earth Planet. Sci. Lett. 393, 165–172.

Stackhouse, S., Stixrude, L., Karki, B.B., 2010. Thermal conductivity of periclase (MgO) from first principles. Phys. Rev. Lett. 104, 208501.

Stackhouse, S., Stixrude, L., Karki, B.B., 2015. First-principles calculations of the lattice thermal conductivity of the lower mantle. Earth Planet. Sci. Lett. 427, 11–17.

Stixrude, L., de Koker, N., Sun, N., Mookherjee, M., Karki, B.B., 2009. Thermodynamics of silicate liquids in the deep Earth. Earth Planet. Sci. Lett. 278, 226–232.

Stixrude, L., Lithgow-Bertelloni, C., 2012. Geophysics of chemical heterogeneity in the mantle. Annu. Rev. Earth Planet. Sci. 40, 569–595.

Vacher, P., Verhoeven, O., 2007. Modelling the electrical conductivity of iron-rich minerals for planetary applications. Planet. Space Sci. 55, 455–466.

Weidelt, P., 1972. The inverse problem of geomagnetic induction. Z. Geophys. 48, 257–289.

Williams, Q., Garnero, E.J., 1996. Seismic evidence for partial melt at the base of Earth's mantle. Science 273, 1528–1530.

Wood, B.J., Nell, J., 1991. High-temperature electrical-conductivity of the lower-mantle phase (Mg, Fe)O. Nature 351, 309–311.

Wysocki, A.L., Sabirianov, R.F., van Schilfgaarde, M., Belashchenko, K.D., 2009. First-principles analysis of spin-disorder resistivity of Fe and Ni. Phys. Rev. B 80, 224423.

Xu, Y.S., Shankland, T.J., Poe, B.T., 2000. Laboratory-based electrical conductivity in the Earth's mantle. J. Geophys. Res., Solid Earth 105, 27865–27875.

Yoshino, T., Kamada, S., Zhao, C.C., Ohtani, E., Hirao, N., 2016. Electrical conductivity model of Al-bearing bridgmanite with implications for the electrical structure of the Earth's lower mantle. Earth Planet. Sci. Lett. 434, 208–219.

Yoshino, T., Yamazaki, D., Ito, E., Katsura, T., 2008. No interconnection of ferropericlase in post-spinel phase inferred from conductivity measurement. Geophys. Res. Lett. 35, L22303.

Zhang, Z., Dorfman, S.M., Labidi, J., Zhang, S., Li, M., Manga, M., Stixrude, L., McDonough, W.F., Williams, Q., 2016. Primordial metallic melt in the deep mantle. Geophys. Res. Lett. 43, 3693–3699.

Ziegler, L.B., Stegman, D.R., 2013. Implications of a long-lived basal magma ocean in generating Earth's ancient magnetic field. Geochem. Geophys. Geosyst. 14, 4735–4742.